

Electronic Supplementary Information

Initial metal-metal bond breakage detected by fs X-ray scattering in the photolysis of $\text{Ru}_3(\text{CO})_{12}$ in cyclohexane at 400 nm

Qingyu Kong*, Mads Laursen, Kristoffer Haldrup, Kasper S. Kjær, Dmitry Khakhulin, Elisa Biasin, Tim B. van Driel, Michael Wulff, Victoria Kabanova, Rodolphe Vuilleumier, Savo Bratos, Martin M. Nielsen, Kelly J. Gaffney, Tsu-Chien Weng*, Michel H. J. Koch

Correspondence to: qingyu.kong@synchrotron-soleil.fr, tsuchien.weng@hpstar.ac.cn

Table of Contents

Quantum chemical (DFT) calculations.....	2
Molecular dynamics (MD) simulations.....	2
Solvent contribution.....	2-3
Single Point Linear Combination Fit (LCF).....	3
Global kinetic fit.....	3- 4
Evaluation of the alternative reaction kinetic model.....	4-5
Fourier Transform.....	5
Figure S1: Geometries of possible intermediates.....	6-7
Figure S2: Transient structures and their difference X-ray scattering intensities.....	8
Figure S3: Solvent signals.....	9
Figure S4: Evolution of χ^2 as a function of time for models M1 and M2.....	10
Figure S5: Plots variation of χ^2 of confidence regions as function of k_1 and k_2	11
Figure S6: DFT Calculated IR absorption spectra.....	12
Figure S7: Time course of concentrations for the two kinetic models.....	13
Figure S8: Difference X-ray scattering intensity $q\Delta S(q,t)$ for the two models.....	14
Figure S9: Solvent kinetics.....	15
Figure S10: Solute-only difference scattering intensities, radial distribution functions...	16
Table S1: Conditions in previous and present experiments	17
Table S2: Ru-Ru bond distances (Å) obtained by least squares refinement	17
References	18

Quantum chemical (DFT) calculations.

To be consistent with previous X-ray solution scattering studies using 100 ps X-ray pulses,¹ the geometries of the starting molecule and of a non-exhaustive list of chemically plausible intermediates calculated previously (Figure S1) were used. The geometry of the new intermediate $\text{Ru}_3(\text{CO})_8(\mu\text{-CO})_3$, which was found indispensable to obtain a good fit at delays above 1.5 ps, was calculated using the same method.

MD simulations.

MD simulations on the solvent-solute interactions (cage structure) were performed using the same methods and program as previously (SI of ref 1) with OPLS all-atom force field on C_6H_{12} .² The all-atom Lennard-Jones potential parameters are listed below:

Solute		
Atom	σ (Å)	4ϵ (kJ/mol)
Ru	2.94	0.42
C	3.86	3.03
O	3.08	2.92

Solvent (C_6H_{12})		
Atom	σ (Å)	4ϵ (kJ/mol)
C	3.5	1.1
H	2.5	0.5

Briefly, one solute molecule ($\text{Ru}_3(\text{CO})_{12}$, $\text{Ru}_3(\text{CO})_{11}(\mu\text{-CO})^*$, $\text{Ru}_3(\text{CO})_{10}(\mu\text{-CO})$, $\text{Ru}_3(\text{CO})_{10}$, $\text{Ru}_3(\text{CO})_8(\mu\text{-CO})_3$, $\text{Ru}_3(\text{CO})_{11}$ with all terminal CO, and CO molecule) was placed in a cubic box with a size of ~ 71.6 Å containing 2048 C_6H_{12} molecules. The simulations were performed at 300 K with a density of 0.781 kg/m³. Periodic boundary conditions were used and the Van der Waals interaction was cut off beyond 11 Å. The solute and solvent molecules were considered as rigid, no further geometry optimizations were applied during the simulations. The systems were equilibrated at 300 K over 200 ps at constant temperature, through coupling to a Nose-Hoover thermostat with a time constant of 0.3 - 0.7 ps, depending on the system. The step size was 0.5 fs; the simulations were performed in the NVT ensemble and the trajectories were followed for up to 1.8 ns.

Solvent contribution.

The solvent response was measured by excitation of an azo-dye³ in C_6H_{12} under identical experimental conditions as for the sample at XPP LCLS. The solvent response has three distinct components: One dominating at delays below 1 ps, one in the range 1-100 ps and one at 1 μs as illustrated in Figure S3a. The signal below 1 ps is the average of the $\Delta S(q,t)$ between 100 fs and 1 ps, and the signal for 1-100 ps is the average of the $\Delta S(q,t)$ between 1 ps and 100 ps. In contrast to the signal at 1-100 ps and 1 μs , the signal below 1 ps has a much broader negative feature around $q = 1.28\text{\AA}^{-1}$ and zero intensity at $q < 1\text{\AA}^{-1}$. This is consistent with previous observation that it takes a few ps for the hot solvent to reach equilibrium,⁴ depending on its properties. The signal below 1 ps in Figure S3a corresponds to C_6H_{12} in non-equilibrium conditions. Figure S3b displays our previous synchrotron results, where C_6H_{12} was heated with an IR laser pulse at 1500 and 1700 nm.^{1,5} The solvent signal at $q > 1.5\text{\AA}^{-1}$ can be approximated as zero. To avoid contamination from the noise of the experimental data, the measured $\Delta S(q,t)$ for the solvent response were smoothed (red curves in Figure S3) using a Savitzky-Golay filter. The 1 μs component is due to thermal expansion which sets in on the ns timescale. For analysis of the present experimental data from 100 fs to 50 ps, we used a linear

combination of the first two solvent components with relative contributions as free fitting parameters for each delay. The weights of the components below 1 ps and 1-100 ps as a function of time are shown in Figure S9.

Single Point Linear Combination Fit (LCF)

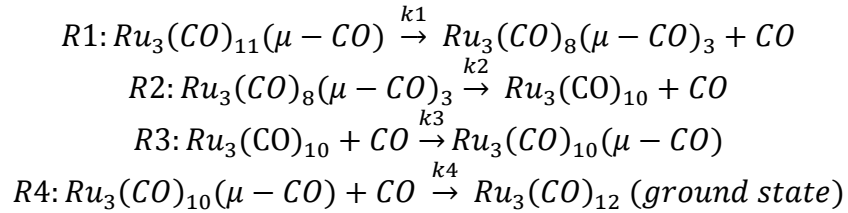
The difference experimental signals, $q\Delta S(q,t)$, at each time delay were fitted using the linear combination fit (LCF) algorithm. The theoretical signals were calculated for candidate solutes listed in Figure S2a plus $\text{Ru}_3(\text{CO})_{11}$ with all terminal CO. Their linear combinations, which include contributions of difference scattering signals of solute, solvent and cage, were compared with the experimental $q\Delta S(q,t)$ (Figure 2B). The strategy was to minimize the figure of merit (χ^2) defined as:

$$\chi^2 = \sum_{i=1}^n \left(\frac{\Delta S_{\text{theory}}(q) - \Delta S_{\text{experiment}}(q)}{\sigma_i} \right)^2 \quad (\text{S1})$$

where σ_i is the standard deviation at a given time-delay, which is obtained from the data reduction procedure⁶ and the summation is over the full q -range. The concentration changes of various chemical species as a function of delay time is obtained by fitting the experimental data at each time delay (170 time points, Figure 2A) separately and plotting the weights corresponding to each species.

Global kinetic fit

The global fitting was performed on the entire set of data in the range from 100 fs to 45 ps. The fitting is based on the kinetic model with four reactions R1-R4 and six different chemical species below:



As no other compounds were detected in our analysis and the difference signal returns to zero after about 1 ms as observed in our previous studies it is legitimate to assume that the yield of each of these reactions is 100%.

The rate equations for the kinetic model are:

$$\begin{aligned} d[\text{Ru}_3(\text{CO})_{12}]/dt &= k_4 [\text{Ru}_3(\text{CO})_{10}(\mu - \text{CO})][\text{CO}] \\ d[\text{Ru}_3(\text{CO})_{11}(\mu - \text{CO})]/dt &= -k_1 [\text{Ru}_3(\text{CO})_{11}(\mu - \text{CO})] \\ d[\text{Ru}_3(\text{CO})_8(\mu - \text{CO})_3]/dt &= k_1 [\text{Ru}_3(\text{CO})_{11}(\mu - \text{CO})] - k_2 [\text{Ru}_3(\text{CO})_8(\mu - \text{CO})_3] \\ d[\text{Ru}_3(\text{CO})_{10}]/dt &= k_2 [\text{Ru}_3(\text{CO})_8(\mu - \text{CO})_3] - k_3 [\text{Ru}_3(\text{CO})_{10}][\text{CO}] \\ d[\text{Ru}_3(\text{CO})_{10}(\mu - \text{CO})]/dt &= k_3 [\text{Ru}_3(\text{CO})_{10}][\text{CO}] - k_4 [\text{Ru}_3(\text{CO})_{10}(\mu - \text{CO})][\text{CO}] \\ d[\text{CO}]/dt &= k_1 [\text{Ru}_3(\text{CO})_{11}(\mu - \text{CO})] + k_2 [\text{Ru}_3(\text{CO})_8(\mu - \text{CO})_3] - k_3 [\text{Ru}_3(\text{CO})_{10}][\text{CO}] - \\ & \quad k_4 [\text{Ru}_3(\text{CO})_{10}(\mu - \text{CO})][\text{CO}] \end{aligned}$$

Given the results of the local fit for the difference signals for individual early time delays below 1 ps it is assumed that $\text{Ru}_3(\text{CO})_{11}(\mu - \text{CO})^*$ is formed instantaneously after excitation, so the initial condition contains a reduced concentration of the parent molecule and a complementary concentration of $\text{Ru}_3(\text{CO})_{11}(\mu - \text{CO})^*$. Once the concentrations kinetics are computed by solving the system of rate equations, the theoretical solute-related difference scattering signal is calculated for each time delay in the experimental data set using the following formula:⁷

$$\Delta S_{solute}^{theor}(q,t) = \sum_i (S_i^{theor}(q,t) \cdot c_i / \sum_k c_k) - S^{theor}_{gs}(q,t) \quad (S2)$$

where c_i is the concentration of the i -th species, $S_i^{theor}(q,t)$ and $S^{theor}_{gs}(q,t)$ are the simulated solute scattering signals for each species and the parent molecule, respectively. The solute scattering signal $S_i^{theor}(q,t)$ includes the contributions from the solute molecule and the component due to the solute-solvent interaction, also known as the cage term. To construct the total predicted difference scattering signals, a sum of the solute and solvent related components was calculated and normalized to one solvent molecule:

$$\Delta S^{theor}(q,t) = 1/R \Delta S_{solute}^{theor}(q,t) + \Delta S_{solvent}(q,t) \quad (S3)$$

where R is the ratio of the numbers of solvent to solute molecules in the solution ($R = 4628$ for a 2 mM solution in C_6H_{12}) and $\Delta S_{solvent}(q,t)$ is the experimentally determined solvent response to the impulsive laser heating scaled to one solvent molecule. The solvent response was measured by excitation of an azo-dye³ in C_6H_{12} under identical experimental conditions as for the sample.

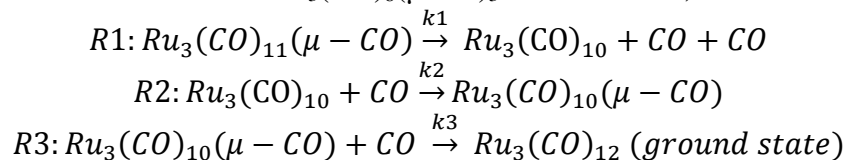
The fitting of experimental data normalized to one solvent molecule was performed using the Matlab[®] implementation of the constrained active-set optimization algorithm to minimize an χ^2 estimator similar to S1:

$$\chi^2 = \sum_{q,t} \left(\frac{\Delta S^{theor}(q,t) - \Delta S^{exp}(q,t)}{\sigma(q,t)} \right)^2 \quad (S4)$$

where the summation is done over all experimental delays, t , in the range from 100 fs to 50 ps and over all values of the momentum transfer, q , in the range from 0.5 to 4.5 \AA^{-1} . Five parameters were optimized in the fitting: the initial concentration of $Ru_3(CO)_{11}(\mu-CO)^*$, and the four rate constants for the reactions R1-R4: k_1 , k_2 , k_3 and k_4 . The initial concentration of $Ru_3(CO)_{11}(\mu-CO)^*$ was constrained during the optimization to be positive and remain below the total concentration of the ground state species before excitation (i.e. 2 mM), while all of the reaction rate constants were forced to be positive and less than $10^{15} \text{ s}^{-1}(\text{M}^{-1})$. The results were insensitive to the last two reaction rate constants k_3 and k_4 , and the optimum is reached as long as $k_3, k_4 < 10^9 \text{ M}^{-1}\text{s}^{-1}$, which confirms previously reported timescales for the R3 and R4 reactions to be in the nanosecond region, i.e. outside of the delay range of the experimental data reported here. For the k_1 and k_2 reaction rate constants, the optimum values were found at $6.6 \pm 0.5 \times 10^{11} \text{ s}^{-1}$ and $1 \pm 0.2 \times 10^{11} \text{ s}^{-1}$ (95% confidence level in both cases), respectively, corresponding to lifetimes of 1.5 ps and 10 ps for $Ru_3(CO)_{11}(\mu-CO)^*$ and $Ru_3(CO)_8(\mu-CO)_3$. Surface plots of variations in the χ^2 and the contour plots of confidence regions as a function of k_1 and k_2 are shown in Figure S5, which illustrates a consistent minimum approached on a smooth surface. The time course of the concentrations for the optimal solution of the kinetic model is presented in Figure 4.

Evaluation of the alternative reaction kinetic model

The triple bridge intermediate $Ru_3(CO)_8(\mu-CO)_3^*$ with M-M bond cleavage is essential for producing an accurate fit of the experimental data. In order to provide statistical validation for this hypothesis we compared the full kinetic model described above with a reduced kinetic model, which does not include the $Ru_3(CO)_8(\mu-CO)_3^*$ intermediate, i.e.:



Since the reduced model (M1) is “nested” in the full kinetic model (M2) a statistical F-test was used to evaluate which model best represents the data. To calculate the probability of the null hypothesis, i.e. that model M2 statistically does *not* fit the data better than model M1, we compute the cumulative distribution function of the probability density function for the F-distribution, p_f , given the numbers of degrees of freedom and values of reduced χ^2_{red} for the respective models:⁸

$$P_F(F_{12}|N-5, N-6) = \int_{F_{12}}^{\infty} p_f \left(F_{12} = \frac{\chi^2_{red}(M1)}{\chi^2_{red}(M2)}, N-5, N-6 \right) \quad (S5)$$

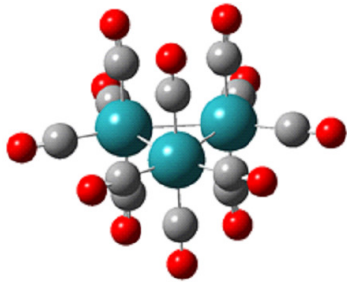
where N is the total number of data points in the relevant data set. The number of degrees of freedom is calculated considering that M1 and M2 have 4 and 5 fitting parameters, respectively. We used the difference scattering data for delays between 300 fs and 5 ps to catch the maximum contribution of the $\text{Ru}_3(\text{CO})_8(\mu\text{-CO})_3^*$ intermediate while still obtaining a good estimate of the concentration of the initially excited $\text{Ru}_3(\text{CO})_{11}(\mu\text{-CO})^*$. The fitting results are $\chi^2_{red}(M1) = 1.85$ and $\chi^2_{red}(M2) = 1.77$. According to (S5) the cumulative probability P_F for our case is only 0.3% allowing to reject the null hypothesis meaning that the full kinetic model M2 represents the experimental data better than the reduced model M1 with 99.7% probability, or “3-sigma” confidence level. The time course of the concentrations for the two kinetic models is shown in Figure S7. The apparent slight difference in the excitation fractions comes from the nature of the kinetic models. In the model M1 the net concentration of species with a broken Ru-Ru bond is smaller and the difference scattering signal is thus smaller, which is partially compensated by a minor increase in the total concentration of the excited state species. Comparison of the fit residuals at 5.16 ps using M1 and M2 as shown in Figure S8 also illustrates that the data is better fitted by M2 with $\text{Ru}_3(\text{CO})_8(\mu\text{-CO})_3^*$ included.

Fourier Transform.

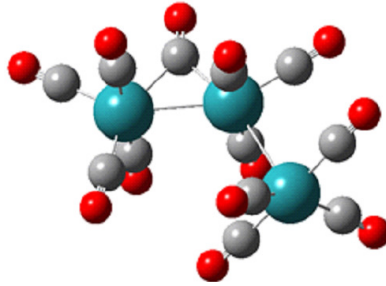
The transform from q to real space (r space) is given by a Fourier sine transform (FT):

$$r\Delta S(r) = \frac{1}{2\pi^2} \int_0^{\infty} q\Delta S(q) \sin(qr) \exp(-q^2\alpha) dq \quad (S6)$$

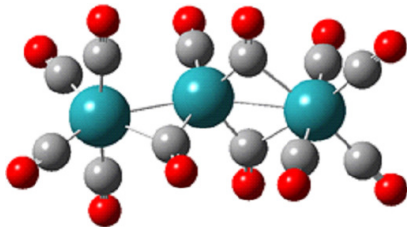
The real $\Delta S(r)$ is convoluted with an exponential function, $\exp(-q^2\alpha)$ to compensate for the limited q -range of the experimental data ($0.5 < q < 4.5 \text{ \AA}^{-1}$). The FTs were carried out with simple numerical integration within the available q -range ($0.5 < q < 4.5 \text{ \AA}^{-1}$), with $\alpha = 0.3$. No sharpening function was applied. The same parameters and processes were applied for all experimental and theoretical data to allow a valid comparison.



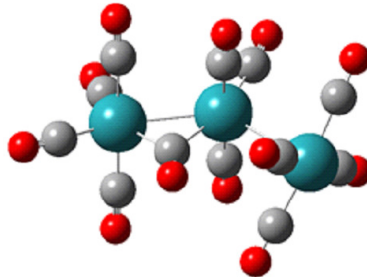
$\text{Ru}_3(\text{CO})_{12}$ ground state, $^1\text{A}_1'$



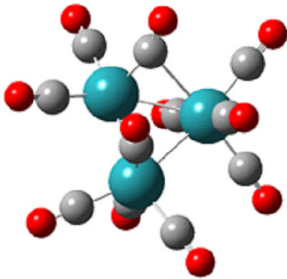
$\text{Ru}_3(\text{CO})_{11}(\mu\text{-CO})$, ^1A



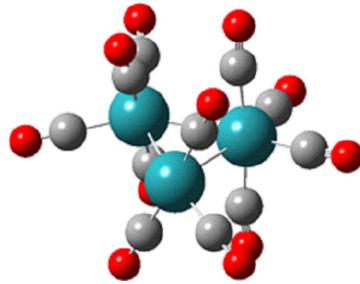
$\text{Ru}_3(\text{CO})_9(\mu\text{-CO})_3$ isomer2, ^1A



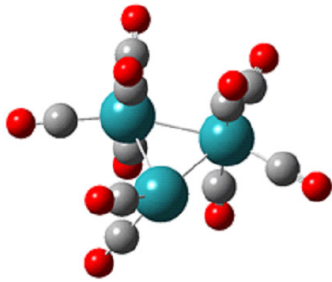
$\text{Ru}_3(\text{CO})_{11}(\mu\text{-CO})$ isomer3, ^1A



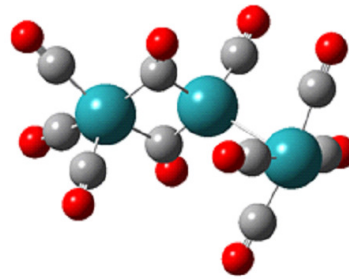
$\text{Ru}_3(\text{CO})_{10}(\mu\text{-CO})$ axial CO loss, ^1A



$\text{Ru}_3(\text{CO})_{11}$ equatorial CO loss, ^1A



$\text{Ru}_3(\text{CO})_{10}$ 2CO loss, ^1A



$\text{Ru}_3(\text{CO})_8(\mu\text{-CO})_2$ 2CO loss, ^1A

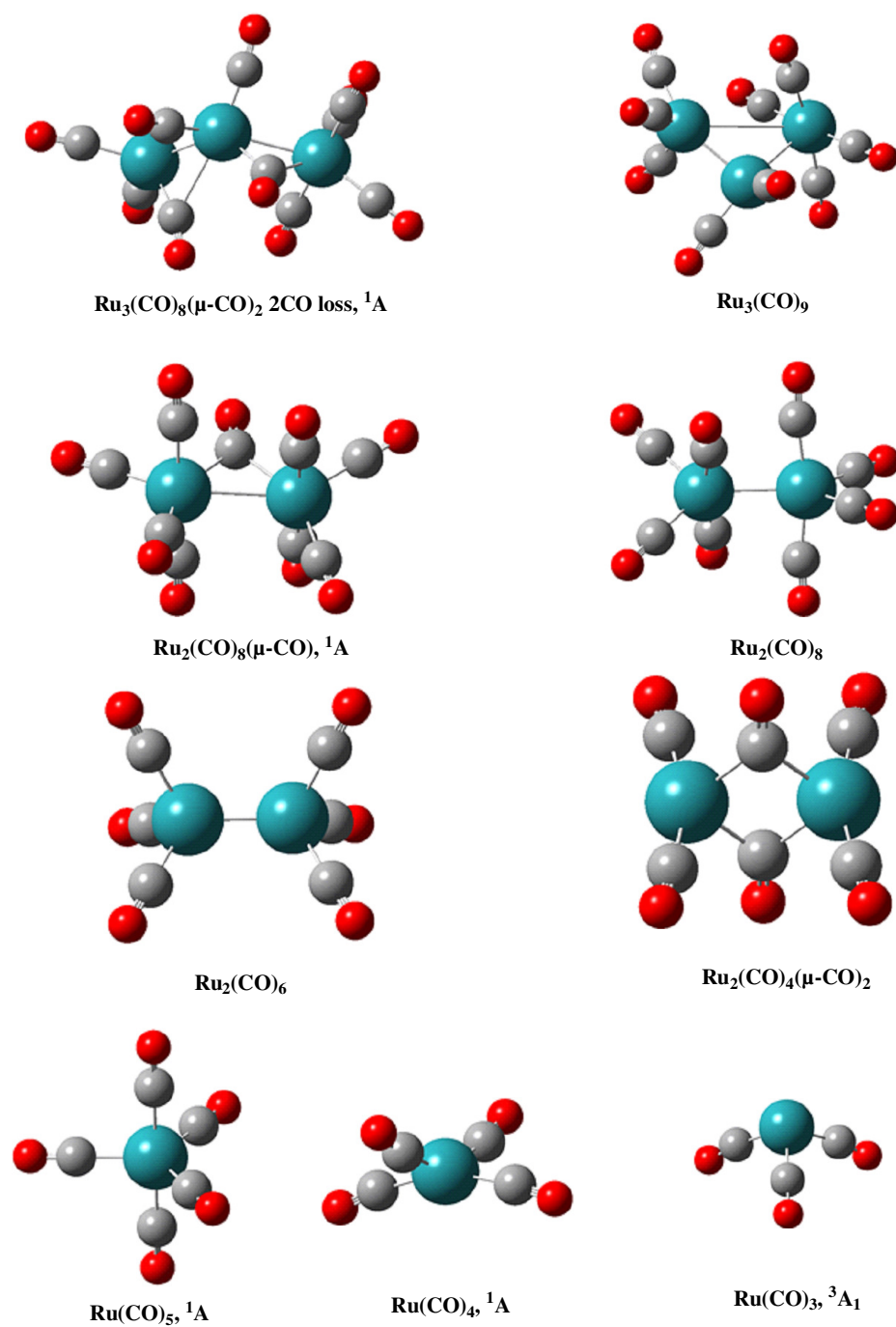


Fig. S1. Geometries of various intermediate molecules obtained using DFT calculations and considered in the data fit. Ru, C, and O atoms are colored in cyan, gray, and red, respectively. Symbols after the name correspond to the symmetry. For the calculations the B3LYP level with the 6-311+G(d) basis set for C and O and Stuttgart RSC 1997 ECP for Ru were used.

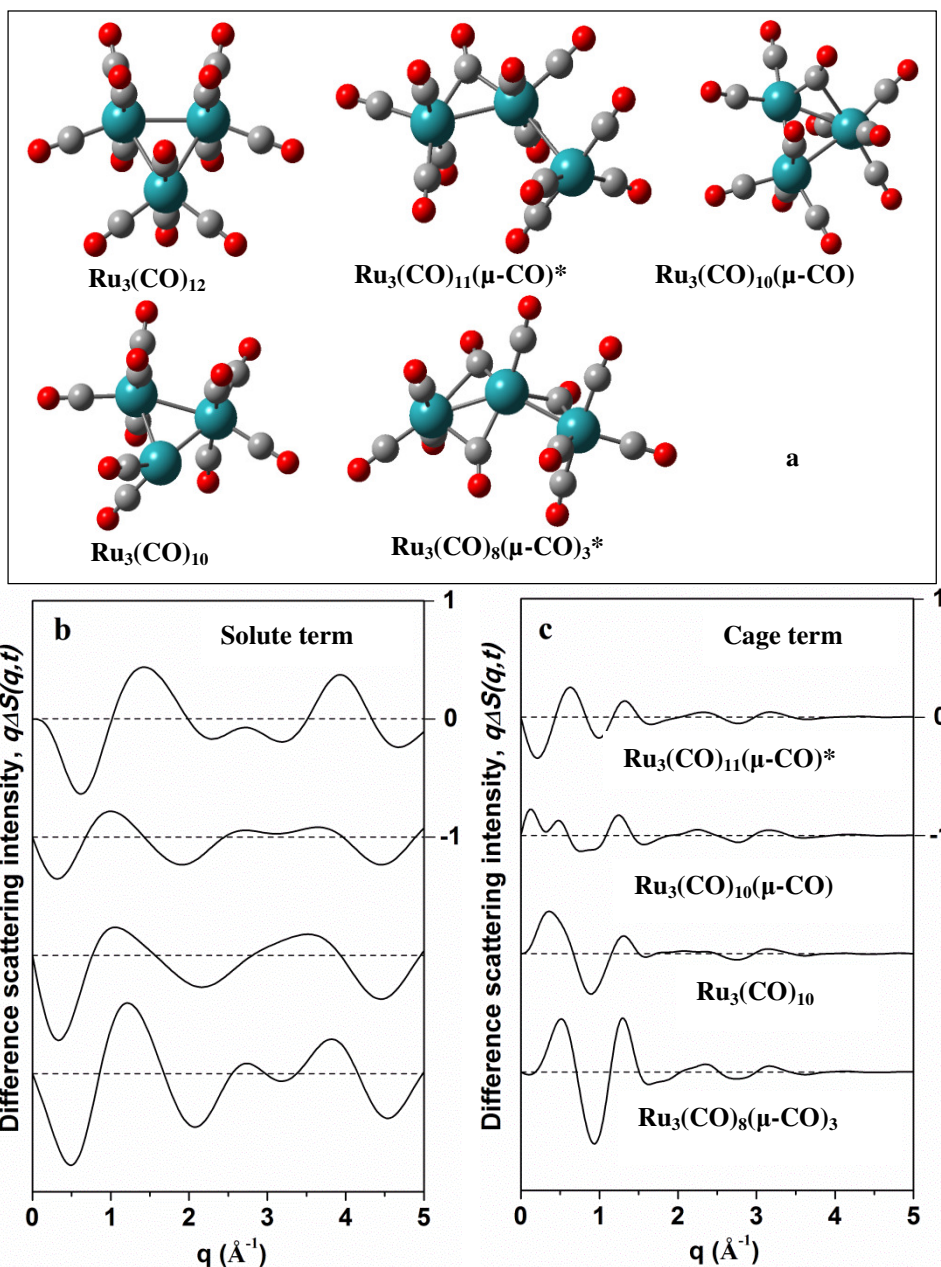


Fig. S2. Transient structures and their difference X-ray scattering intensities. **a**, Transient structures formed after photolysis of $\text{Ru}_3(\text{CO})_{12}$ in C_6H_{12} at 400 nm. $\text{Ru}_3(\text{CO})_{11}(\mu\text{-CO})^*$ with Ru-Ru bond cleavage and one bridged CO is the only species detected 100 fs after laser excitation. $\text{Ru}_3(\text{CO})_{10}(\mu\text{-CO})$ with one bridged CO was identified previously by ultrafast IR and 100 ps resolution X-ray scattering. $\text{Ru}_3(\text{CO})_{10}$ with terminal CO only is the major photoproduct previously observed by 100 ps resolution X-ray scattering. $\text{Ru}_3(\text{CO})_8(\mu\text{-CO})_3^*$ with Ru-Ru bond cleavage and three bridged CO is a new species identified by fs X-ray scattering. **b**, Difference X-ray scattering intensities $q\Delta S(q,t)$ of the intermediates i.e. differences between the scattering patterns of the intermediate and the parent molecule $\text{Ru}_3(\text{CO})_{12}$ calculated using analytical functions for the atomic scattering factors.⁹ **c**, Corresponding differences for the cage structures from MD simulations. The Ru_3 ring and all CO ligands were included in the calculation of the X-ray scattering signals. The $q\Delta S(q,t)$ in **b** and **c** were scaled to one solvent molecule according to the ratio of the numbers of solvent to solute molecules (R) in the solution ($R = 4628$ for a 2 mM solution in C_6H_{12}).

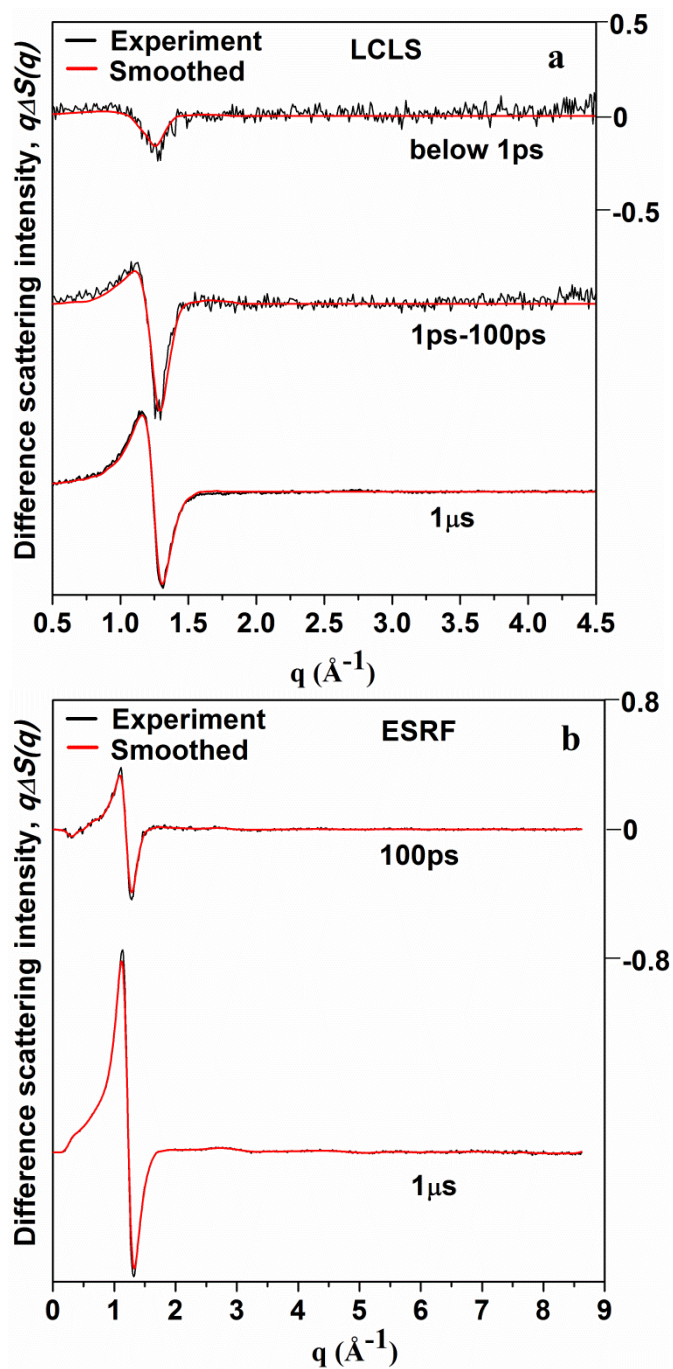


Fig. S3. Solvent signals. **a**, The solvent response was measured by excitation of an azo-dye³ in C₆H₁₂ under identical experimental conditions as for the sample at XPP LCLS. **b**, Impulsive heating of pure C₆H₁₂ using IR laser pulses (signal and idle from the Topas laser at 1500 nm and 1700 nm) at ID09 ESRF. The curves have been shifted vertically for better visualization.

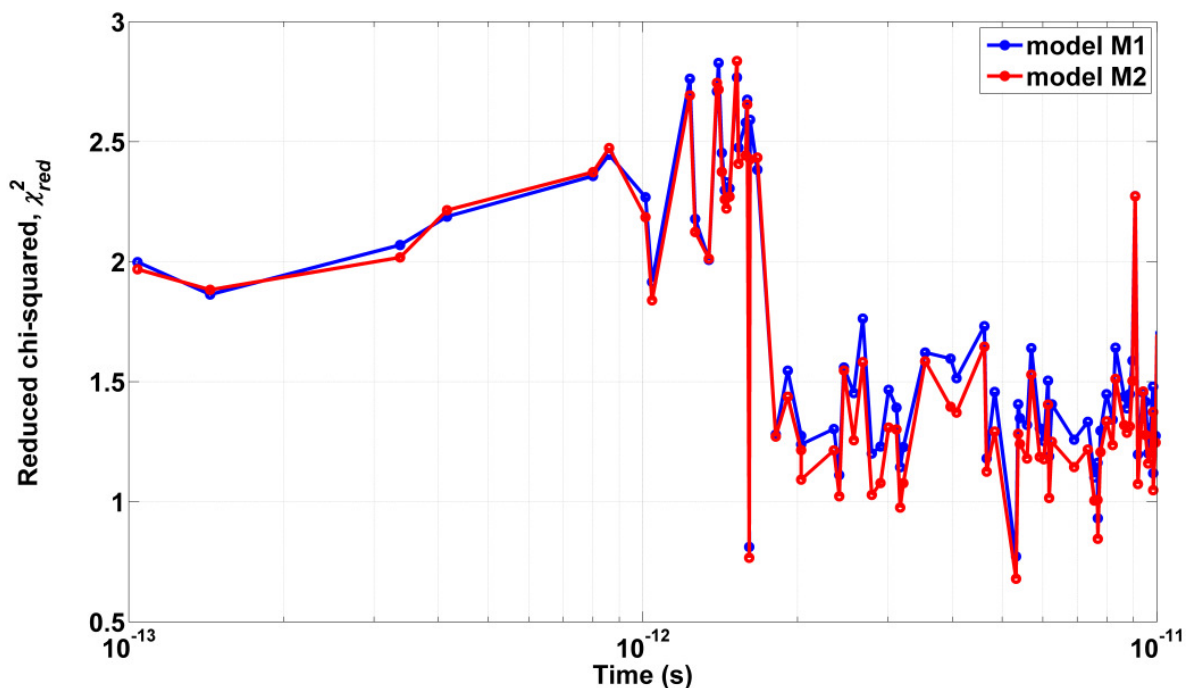


Fig. S4: Evolution of χ^2 as a function of time for models M1 and M2. The sharp drop near 1 ps reflects the fact that when they cool down the excited molecules have a geometry that is closer to that of the models. Studies of the vibrational cooling dynamics of metal carbonyls¹⁰ suggest that the cooling process for CO vibrations may take up to tens of ps, although the main effects occur at times below 1 ps. It can be assumed that the hot vibrational bands are mainly the CO stretches involving light atoms to which X-ray scattering is less sensitive. The difference signal below 1 ps may thus also contain a contribution from excited $\text{Ru}_3(\text{CO})_{12}$ molecules. Lower frequency modes such as those of Ru-Ru bonds tend to redistribute faster to the solvent. The fit with M2 is systematically better than that of M1. The lower χ^2 values correspond to the region where the contribution of $\text{Ru}_3(\text{CO})_8(\mu\text{-CO})_3^*$ dominates.

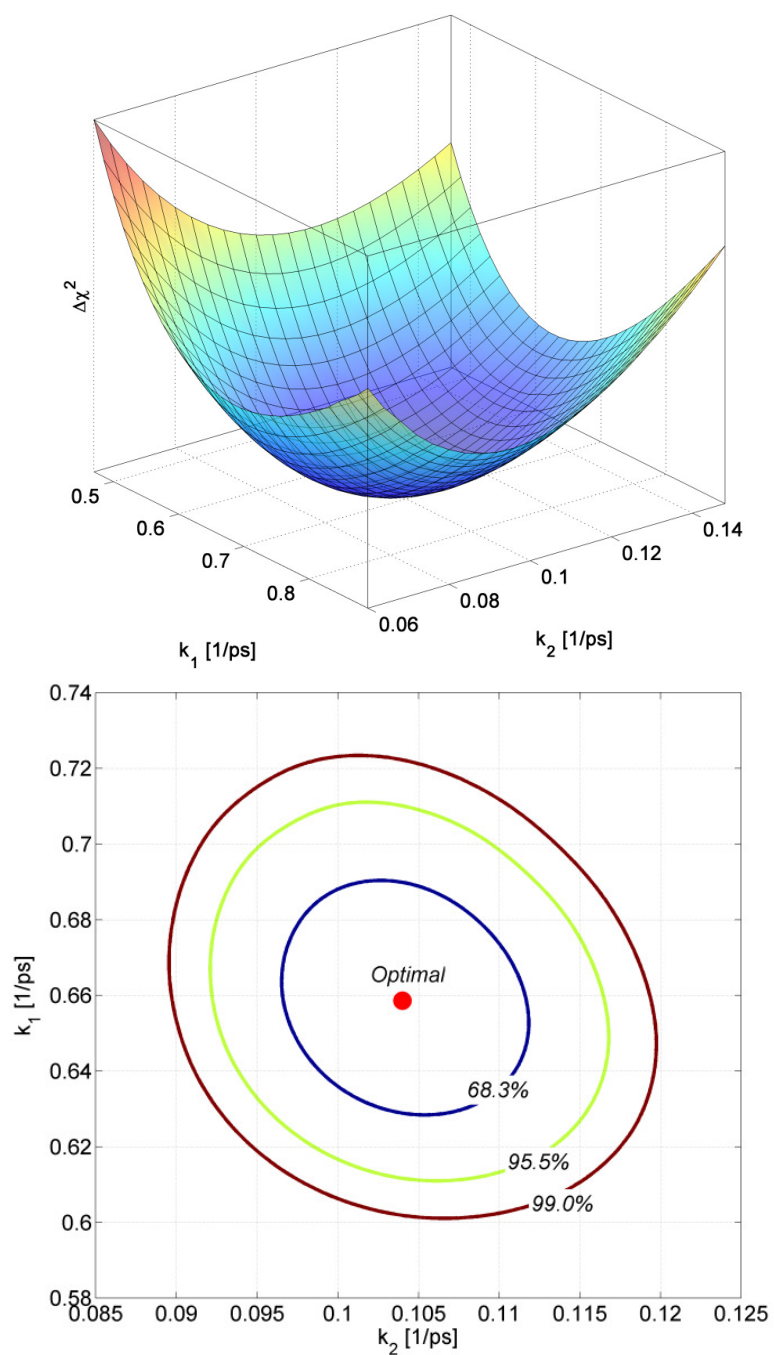


Fig. S5. Surface plots of variations in the χ^2 and the contour plots of confidence regions as a function of k_1 and k_2 . χ^2 surface (top) and respective contour plots (bottom) showing the confidence regions in the space of the k_1 and k_2 reaction rate constants.

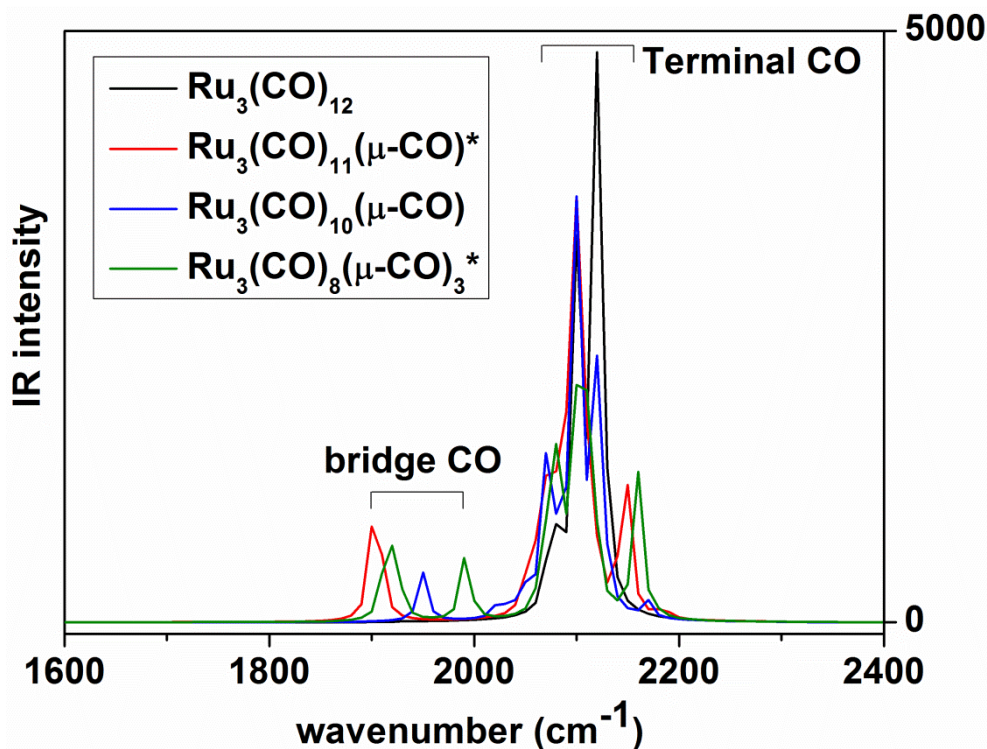


Fig. S6. DFT Calculated IR absorption spectra. $\text{Ru}_3(\text{CO})_{12}$ (black), $\text{Ru}_3(\text{CO})_{11}(\mu\text{-CO})^*$ (red), $\text{Ru}_3(\text{CO})_{10}(\mu\text{-CO})$ (blue) and $\text{Ru}_3(\text{CO})_8(\mu\text{-CO})_3^*$ (olive). Calculated absorption bands from the stretching mode of bridged COs are 1888.65 cm^{-1} for $\text{Ru}_3(\text{CO})_{11}(\mu\text{-CO})^*$, 1934.07 cm^{-1} for $\text{Ru}_3(\text{CO})_{10}(\mu\text{-CO})$ and 1889.41 , 1899.71 and 1969.79 cm^{-1} for $\text{Ru}_3(\text{CO})_8(\mu\text{-CO})_3^*$. The first two bands of $\text{Ru}_3(\text{CO})_8(\mu\text{-CO})_3^*$ are highly overlapped with the absorption of $\text{Ru}_3(\text{CO})_{11}(\mu\text{-CO})^*$, the band at 1969.79 cm^{-1} is close to those of terminal CO, which is probably why $\text{Ru}_3(\text{CO})_8(\mu\text{-CO})_3^*$ escaped detection in previous time-resolved IR study.¹¹ The IR frequency was calculated using B3LYP function, with 6-311+G(3df,3pd) basis set for C and O, and Stuttgart-Koeln MCDHF RSC ECP basis set for Ru.

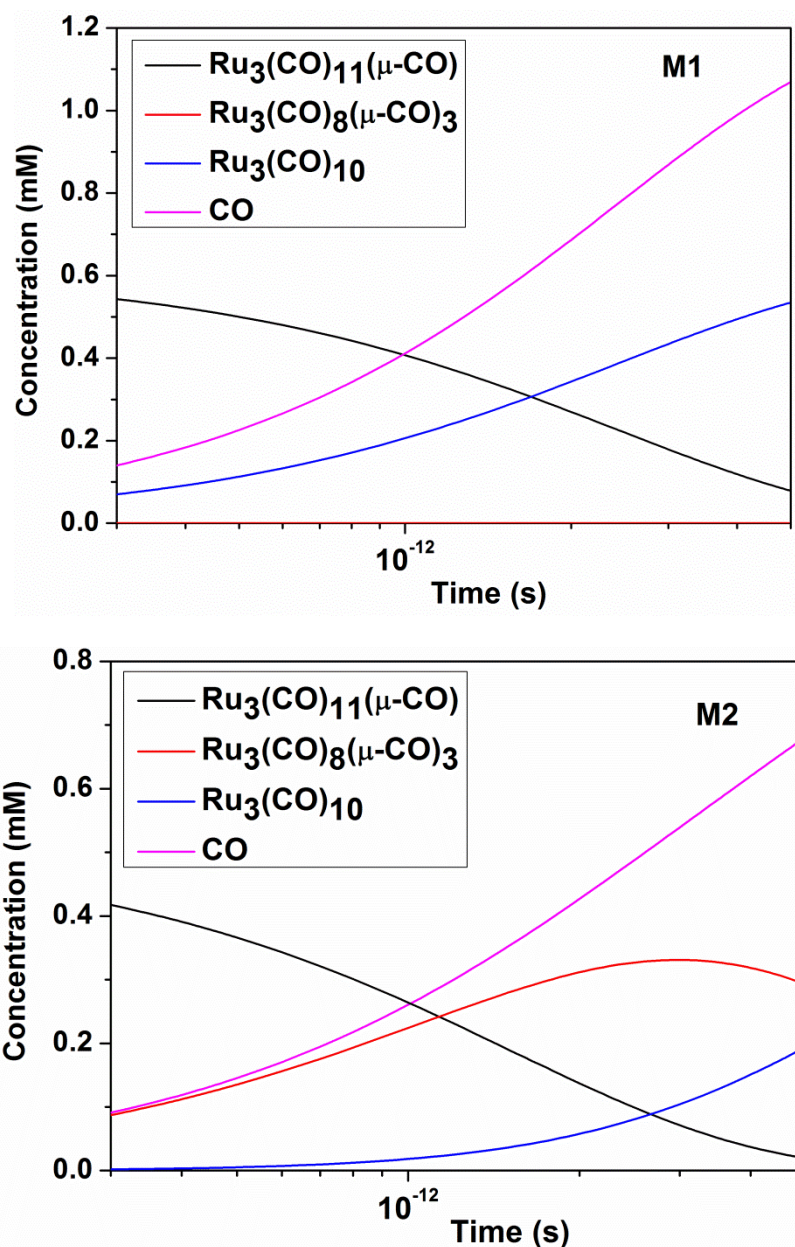


Fig. S7. Time course of concentrations for the two kinetic models without (M1) and with (M2) $\text{Ru}_3(\text{CO})_8(\mu\text{-CO})_3^*$ between 300 fs and 5 ps.

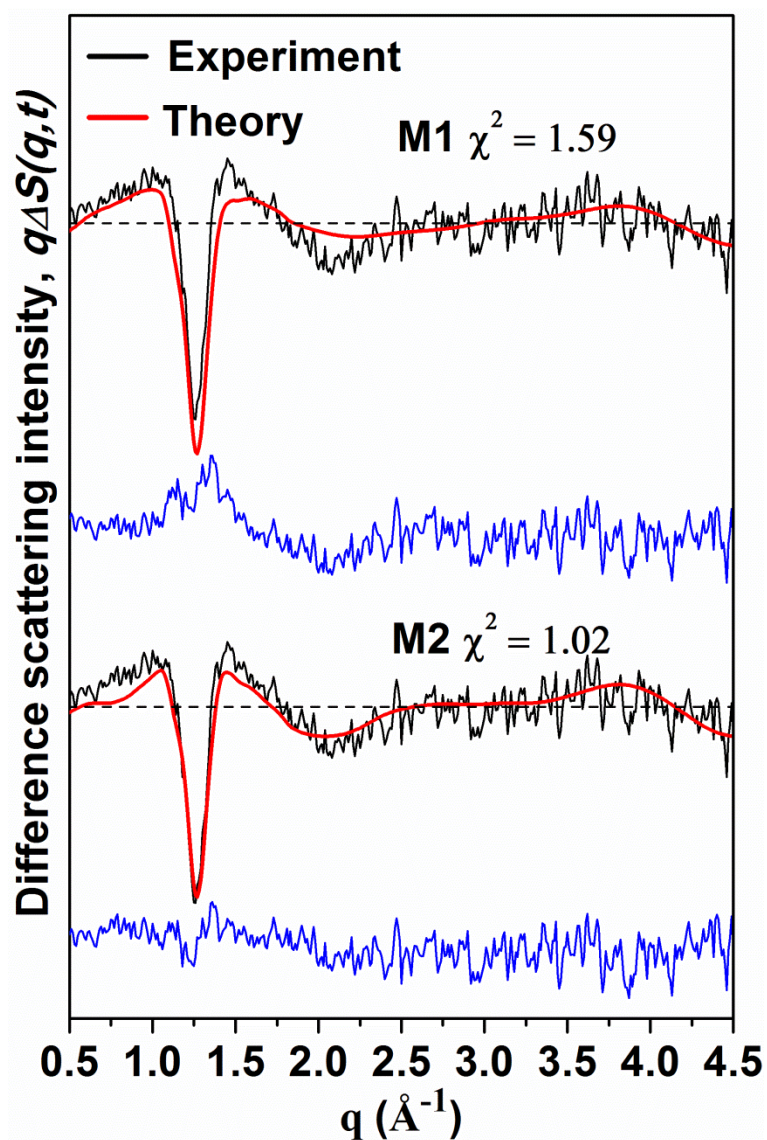


Fig. S8. Comparison of experimental difference X-ray scattering intensity $q\Delta S(q,t)$ with **M1** and **M2**. $q\Delta S(q,t)$ at 5.16 ps (black) compared with M1 and M2 (red), the blue curves are the difference between the experimental data and the theoretical curves. M2 with $\text{Ru}_3(\text{CO})_8(\mu\text{-CO})_3^*$ represents the data significantly better especially in the range $1.0 < q < 2.5 \text{ \AA}^{-1}$ where both the difference X-ray scattering intensity of $\text{Ru}_3(\text{CO})_8(\mu\text{-CO})_3^*$ and its cage contribute, as illustrated in Figure S2b,c.

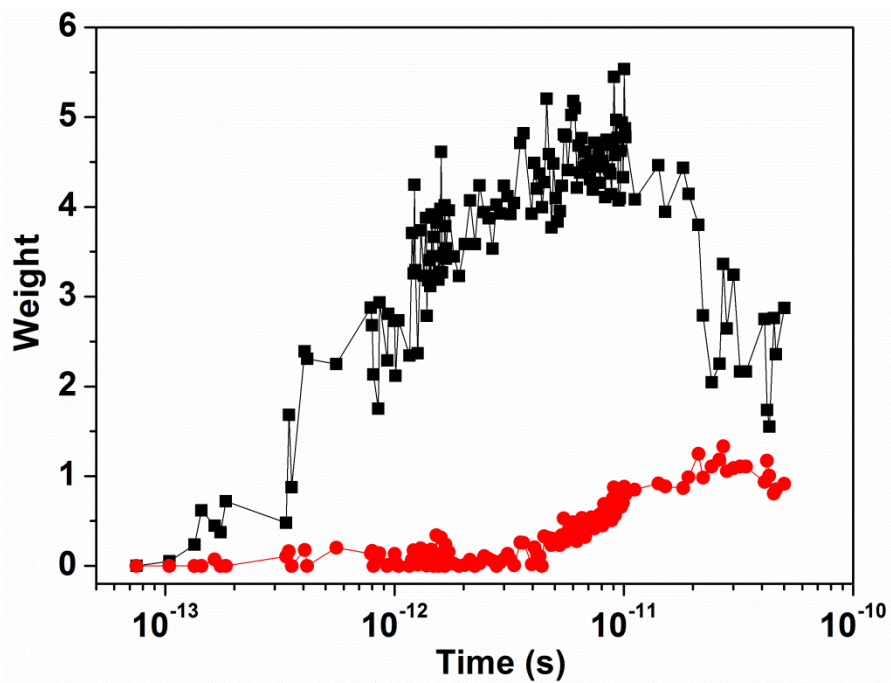


Fig. S9. Solvent kinetics. Time course of the weight of the solvent contribution below 1 ps (black) and 1 – 100 ps (red).

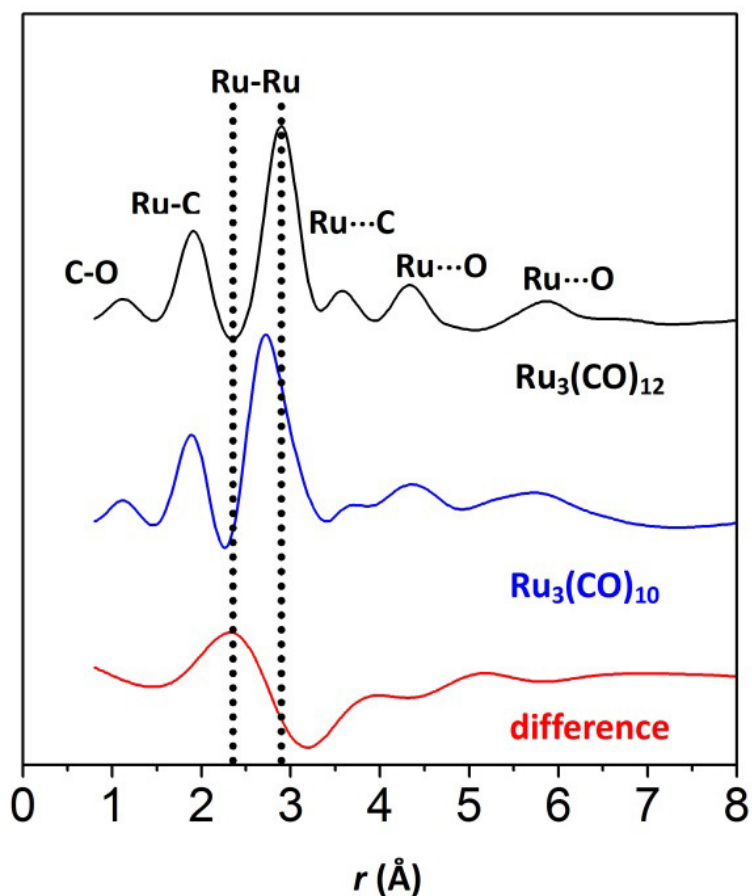


Fig. S10. Radial distribution functions (RDFs). The RDFs of $\text{Ru}_3(\text{CO})_{12}$ at ground state (black), $\text{Ru}_3(\text{CO})_{10}$ (blue), and the difference RDF (red) between $\text{Ru}_3(\text{CO})_{10}$ and the ground state. The dashed lines show the positions of the Ru-Ru peaks from difference (red) and ground state (black). It is clear that the positive peak in the difference RDF around 2.4 Å corresponds to the average Ru-Ru distance in $\text{Ru}_3(\text{CO})_{10}$ shifts to a shorter distance, while the negative hole around 3.2 Å correspond to the broken Ru-Ru bond compared to the parent molecule shifts to a longer distance, producing a “Mexican hat profile”. The RDFs of $\text{Ru}_3(\text{CO})_{12}$ at ground state and $\text{Ru}_3(\text{CO})_{10}$ were obtained by sine-Fourier transformation of the difference between the Debye and the equivalent atomic scattering of each molecule.⁵

Table S1. Conditions in previous and present experiments

Source	Pump pulse length	Probe pulse length	Pump spot size (μm)	Pump energy (μJ)	Pump power density $\text{J}(\text{s}\cdot\mu\text{m}^2)^{-1}$
IR ¹¹	100 fs	150 fs	100	1.6	2038
ESRF ¹	1 ps	100 ps	150	60	3397
XTA ¹²	5 ps	100ps	800	220	275
LCLS	30 fs	40 fs	100	14	59445

Table S2. Ru-Ru bond distances (\AA) obtained by least squares refinement of the time-resolved X-ray scattering data and DFT (*I*).

Species	Experiment ^[a,b]	DFT
$\text{Ru}_3(\text{CO})_{12}$ ^[c]	Ru1-Ru2: 2.88	2.93
	Ru1-Ru3: 2.88	2.93
	Ru2-Ru3: 2.88	2.93
$\text{Ru}_3(\text{CO})_{11}(\mu\text{-CO})^*$	<i>Ru1-Ru2: 2.86</i>	<i>2.91</i>
	<i>Ru1-Ru3: 5.05</i>	<i>5.14</i>
	<i>Ru2-Ru3: 3.12</i>	<i>3.17</i>
$\text{Ru}_3(\text{CO})_{10}(\mu\text{-CO})$	Ru1-Ru2: 2.76	2.81
	Ru1-Ru3: 2.89	2.94
	Ru2-Ru3: 2.79	2.84
$\text{Ru}_3(\text{CO})_{10}$	Ru1-Ru2: 2.66	2.71
	Ru1-Ru3: 2.89	2.94
	Ru2-Ru3: 2.68	2.73
$\text{Ru}_3(\text{CO})_8(\mu\text{-CO})_3^*$	<i>Ru1-Ru2: 2.73</i>	<i>2.78</i>
	<i>Ru1-Ru3: 2.83</i>	<i>2.88</i>
	<i>Ru2-Ru3: 5.18</i>	<i>5.27</i>

[a] A single scale factor was refined and used to scale all DFT values. [b] The actual errors associated with the fits are smaller than the last digit. [c] The experimental values for $\text{Ru}_3(\text{CO})_{12}$ are close to those in the crystal structure (2.86, 2.85, 2.85 \AA).¹³ The Ru-Ru bond distances in **$\text{Ru}_3(\text{CO})_{11}(\mu\text{-CO})^*$** and **$\text{Ru}_3(\text{CO})_8(\mu\text{-CO})_3^*$** were scaled from DFT calculations.

References

- 1 Q. Y. Kong, J. H. Lee, H. Plech, M. Wulff, H. Ihee and M. H. J. Koch, *Angew. Chem. Int. Ed.*, 2008, **47**, 5550.
- 2 W. L. Jorgensen, D. S. Maxwell and J. Tirado-Rives, *J. Am. Chem. Soc.*, 1996, **118**, 11225.
- 3 K. S. Kjær, T. B. van Driel, J. Kehres, K. Haldrup, D. Khakhulin, K. Bechgaard, M. Cammarata, M. Wulff, T. J. Sorensen and M. M. Nielsen, *Phys. Chem. Chem. Phys.*, 2013, **15**, 15003.
- 4 K. S. Kjær, *Ph.D Thesis, The Graduate School of Science, Faculty of Science, Niels Bohr Institute, University of Copenhagen Denmark*, 2013.
- 5 Q. Y. Kong, J. H. Lee, K. H. Kim, J. H. Kim, M. Wulff, H. Ihee and M. H. J. Koch, *J. Am. Chem. Soc.*, 2010, **132**, 2600.
- 6 T. B. Van Driel, K. S. Kjær, R. W. Hartsock, A. O. Dohn, T. Harlang, M. Chollet, M. Christensen, W. Gawelde, N. E. Henriksen, J. G. Kim, K. Haldrup, K. H. Kim, H. Ihee, J. Kim, H. T. Lemke, Z. Sun, V. Sundstrom, W. K. Zhang, D. L. Zhu, K. B. Moller, M. M. Nielsen and K. J. Gaffney, *Nat. Commun.*, 2016, **7**, 13678.
- 7 H. Ihee, M. Lorenc, K. Kim, Q. Y. Kong, M. Cammarata, J. H. Lee, S. Bratos and M. Wulff, *Science*, 2005, **309**, 1223.
- 8 P. R. Bevington and D. K. Robinson, *McGraw Hill, New York, NY*, 2003.
- 9 D. Waasmaier and A. Kirfel, *Acta Cryst.*, 1995, **A51**, 416.
- 10 J.C. King, J.Z. Zhang, B.J. Schwartz and C.B. Harris, *J. Phys. Chem.*, 1993, **99**, 7595.
- 11 E. A. Glascoe, M. F. Kling, J. E. Shanoski and C. B. Harris, *Organometallics*, 2006, **25**, 775.
- 12 M. R. Harpham, A. B. Stickrath, X. Y. Zhang, J. Huang, M. W. Mara, L. X. Chen and D. J. Liu, *J. Phys. Chem. A*, 2013, **117**, 9807.
- 13 M. R. Churchill, F. J. Hollander and J. P. Hutchinson, *Inorg. Chem.* 1977, **16**, 2655.